Realizing Synergy between In$_2$O$_3$ Nanocubes and Nitrogen-Doped Reduced Graphene Oxide: An Excellent Nanocomposite for the Selective and Sensitive Detection of CO at Ambient Temperatures

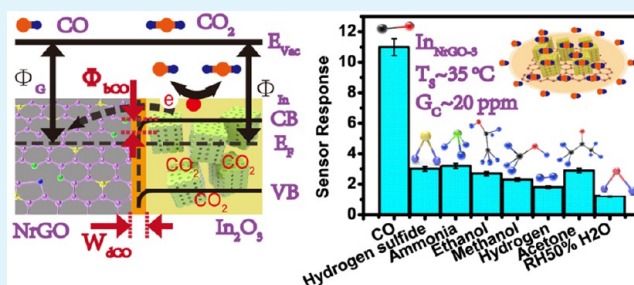Arunkumar Shanmugasundaram,[†] Veerabrahmachari Gundimeda,[‡] Tianfeng Hou,[†] and Dong Weon Lee*,[†]

[†]MEMS and Nanotechnology Laboratory, School of Mechanical Systems Engineering, Chonnam National University, Gwangju-61186, Republic of Korea

[‡]Nanomaterials Laboratory, Inorganic and Physical Chemistry Division, CSIR-Indian Institute of Chemical Technology, Hyderabad-500 007, Telangana, India

S *Supporting Information*

ABSTRACT: Hierarchical mesoporous In$_2$O$_3$ nanocubes and nitrogen-doped reduced graphene oxide–indium oxide nanocube (In$_{NrGO}$) composites were prepared for carbon monoxide (CO) sensing. The as-synthesized materials were systematically investigated by different characterization techniques such as field emission scanning electron microscopy, transmission electron microscopy, X-ray diffraction, thermogravimetic analysis, X-ray photoelectron spectroscopy, micro-Raman, Fourier transform infrared spectroscopy, and photoluminesce analysis. The obtained results are consistent with each other. The CO-sensing characteristics of the In$_2$O$_3$ nanocubes and In$_{NrGO}$ composites were examined at different operating temperatures (35 °C < T_s < 300 °C) and CO concentrations (1−1000 ppm). Owing to their large surface-to-volume ratio and porosity, the In$_2$O$_3$ nanocubes exhibited a superior sensitivity with a detection limit of 1 ppm at 250 °C. Furthermore, to enhance the sensing characteristics and reduce the operating temperature, a composite of NrGO and In$_2$O$_3$ nanocubes was fabricated. The incorporation of NrGO drastically improved the sensing performance of the In$_2$O$_3$ nanocubes, showing an excellent sensitivity ($S_R \sim$ 3.6−5 ppm of CO at $\sim$35 °C) with appreciably fast response ($\Gamma_{RES} \sim$ 22 s) and recovery ($\Gamma_{REC} \sim$ 32 s) times. The sensing studies supported by the structural and morphological material characteristics lead to the plausible sensing mechanism proposed.

KEYWORDS: NrGO, indium oxide, hybrid nanocomposite, room-temperature CO detection, highly sensitive

INTRODUCTION

In the current situation of global health awareness and pollution norms, environmental monitoring and the safeguarding of human health is of prime importance, and sensors can play a significant role in these areas. Air pollutants are major concerns to human health and other environmental issues.[1,2] Among various air pollutant gases, CO is one of the most toxic, as its inhalation leads to the depletion or diminution of oxygen in animal tissues. CO is a colorless, odorless, and tasteless gas; therefore, it is hard to detect. CO poisoning causes headache, nausea, dizziness, and confusion, and exposure to high concentrations may result in death.[3,4] Therefore, an effective sensor for early detection with fast response time to low concentrations of CO at ambient temperatures is crucial for ensuring safety in industrial environments.

Gas sensors based on metal oxide semiconducting nanomaterials have attracted significant research interest.[5−9] Among several metal oxides, In$_2$O$_3$ has received significant attention as a potential gas-sensing material, and its response to various toxic and combustible volatile organic compounds (VOCs) has

been investigated. However, a drawback associated with In$_2$O$_3$-based gas sensors is their high operating temperatures. For example, Neri et al. prepared hierarchical In$_2$O$_3$ materials and studied their CO gas-sensing behaviors at 250 °C.[10] Lim et al. prepared mesoporous In$_2$O$_3$ nanofibers by an electrospinning method and achieved enhanced CO sensitivity at 300 °C.[11]
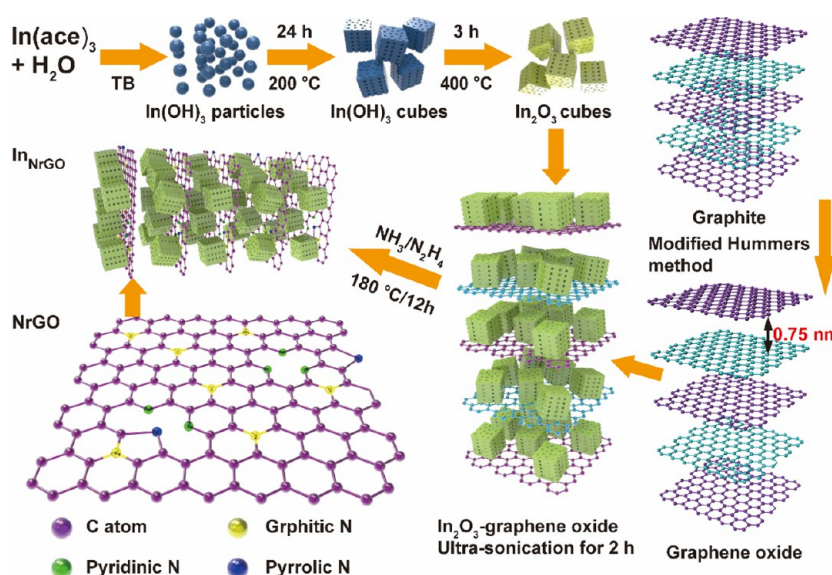
Over the past few years, significant research efforts have been directed to improving the sensitivity of the sensors by employing various approaches.[12] Recently, Lee suggested that hierarchical structures can lead to enhanced sensing properties, including high sensitivity and substantially improved response and recovery times. The author also noted that a porous structure provides numerous channels for gas diffusion, presenting high accessible active sites for the chemisorption of gases.[13] The best and most widely accepted method to decrease the operating temperature and improve the sensing

Scheme 1. Illustration of the Synthesis of Mesoporous In$_2$O$_3$ Nanocubes and Nitrogen-Doped Reduced Graphene Oxide−In$_2$O$_3$ Nanocube Composites

characteristics relies on the incorporation of metal nano-particles into metal oxide matrices.[14−18] In general, nanosized gold is an efficient catalyst for CO oxidation at lower operating temperatures. For instance, Fu et al. prepared rodlike Au/In$_2$O$_3$ nanocomposites and demonstrated their utility as sensitive CO sensors at room temperature.[19] However, using precious metals is not advantageous from an economic perspective, owing to their higher price. As a result, there have been extensive ongoing investigations to identify efficient, durable, and inexpensive alternative catalysts for CO oxidation.

Currently, the incorporation of reduced graphene oxide (rGO) into metal oxides is considered an effective route to improve the efficiency of gas-sensing materials because of its enhanced gas adsorption capacity, chemically active defect sites, high conductivity, and outstanding charge-carrier mobility.[20,21] rGO has been incorporated with several metal oxides, and the resultant composites have been successfully demonstrated to efficiently sense several target gases.[22−28] However, the sensing properties of rGO−metal oxide composites to CO gas detection have not been well-studied. Furthermore, theoretical studies have revealed that chemical doping with catalytically active materials can enhance the catalytic and electrical properties of rGO, rendering them much more sensitive to CO compared to pristine graphene.[29,30] Among the different dopants tried for rGO, nitrogen (N) because of its proximity to C is highly preferred because of the size equivalence and the five valence electrons that are easily amenable for bonding with carbon.[31] Previous reports suggest that N-graphene presents more versatile properties compared to pristine graphene. For example, nitrogen doping enhances the graphene metallic nature, affects the lattice alignment, and creates several "active regions" by influencing the charge distribution of the carbon atoms. This type of "active region" can effectively increase catalytic reactions, as has been experimentally proven in reactions such as hydrogen evolution, oxygen evolution, and oxygen reduction.[32,33]

With this background, and considering the advantages of the excellent properties of In$_2$O$_3$ and NrGO, we prepared a new type of composite based on N-doped reduced graphene oxide and indium oxide (In$_{NrGO}$) for ultrasensitive CO detection.

Gas-sensing studies revealed that the NrGO composite shows improved sensing characteristics over pristine rGO. The In$_{NrGO}$ sensing material was prepared via a three-step synthetic process. First, In$_2$O$_3$ nanocubes were prepared under hydrothermal conditions using indium acetate and Trizma base. Next, graphene oxide was prepared by a modified Hummers's method. Finally, the In$_{NrGO}$ composites were prepared under hydrothermal conditions at 180 °C using ammonia/hydrazine hydrate as the nitrogen source. To optimize the sensing characteristics, different weight percentages of NrGO were incorporated with In$_2$O$_3$ nanocubes, and the composites were named as In$_{NrGO-1}$, In$_{NrGO-2}$, and In$_{NrGO-3}$. The CO-sensing characteristics of the In$_2$O$_3$ and In$_{NrGO}$ composites were studied as a function of the gas concentration (1 ppm < G_c < 1000 ppm) at different operating temperatures (35 °C < T_s < 300 °C). Owing to the large surface area (71.6 m^2·g^{-1}) and high porosity, the as-prepared In$_2$O$_3$ nanocrystals exhibit an enhanced sensor response (S_R ∼ 82−100 ppm of CO at 250 °C) with a sensitivity as low as 1 ppm. Meanwhile, the In$_{NrGO-3}$ composite exhibits a superior sensing response of S_R ∼ 273 at 175 °C and S_R ∼ 53.4 at room temperature (T_S ∼ 35 °C) to 100 ppm of CO. The fabricated sensor also shows excellent sensitivity (5 ppm; S_R ∼ 3.78) and selectivity to CO at room temperature.

■ EXPERIMENTAL SECTION

Chemicals. Graphite flakes (+100 mesh), sulfuric acid (H$_2$SO$_4$), nitric acid (HNO$_3$), hydrazine hydrate (NH$_2$NH$_2$), ammonia solution (NH$_3$), indium(III) acetate dihydrate (In(C$_2$H$_3$O$_2$)$_3$·2H$_2$O), and Trizma base (NH$_2$C(CH$_2$OH)$_3$) were purchased from Sigma-Aldrich Chemical Co. All the chemicals were of analytical reagent (AR) grade and used without further purification.

Preparation of Mesoporous Indium Hydroxide (In(OH)$_3$) Nanocubes. First, indium acetate dihydrate (0.483 g) was dissolved in 50 mL of deionized water under continuous stirring, followed by the addition of Trizma base (0.969 g). After 15 min of stirring, the resulting mixture was poured into a Teflon-lined stainless autoclave and heated at 200 °C for 24 h. Subsequently, the autoclave was naturally cooled to room temperature. The obtained product was purified with deionized water and ethanol by centrifugation, then dried at 80 °C.
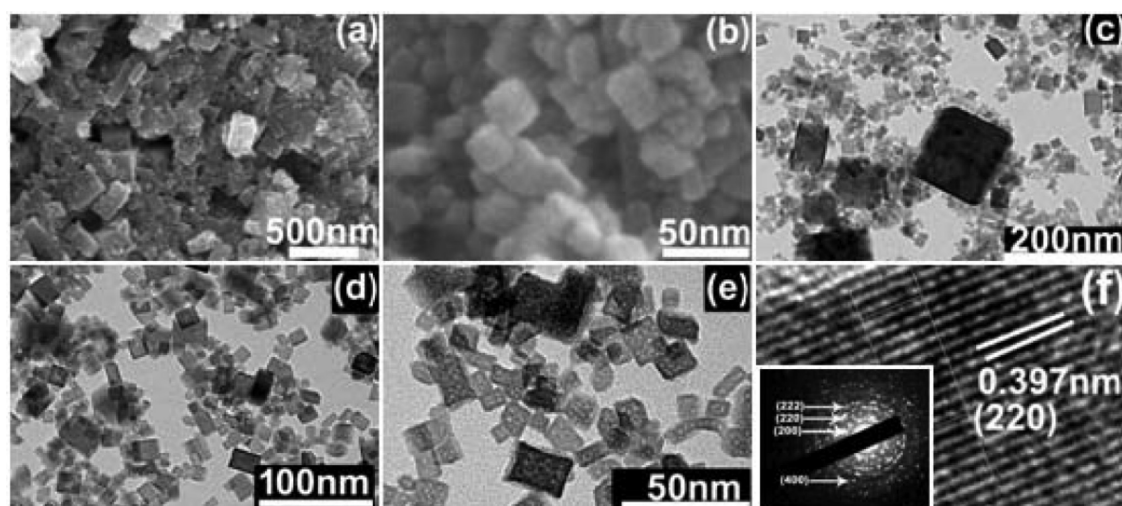
Figure 1. Electron microscopy images of the as-prepared $In(OH)_3$ nanocubes in scanning and transmission modes. Representative FESEM images of the $In(OH)_3$ nanocubes at (a) low and (b) high magnification; (c−e) TEM images of the $In(OH)_3$ nanocubes at different magnifications; (f) a high-resolution TEM image of the as-prepared $In(OH)_3$ nanocubes; inset: selected area electron diffraction pattern.
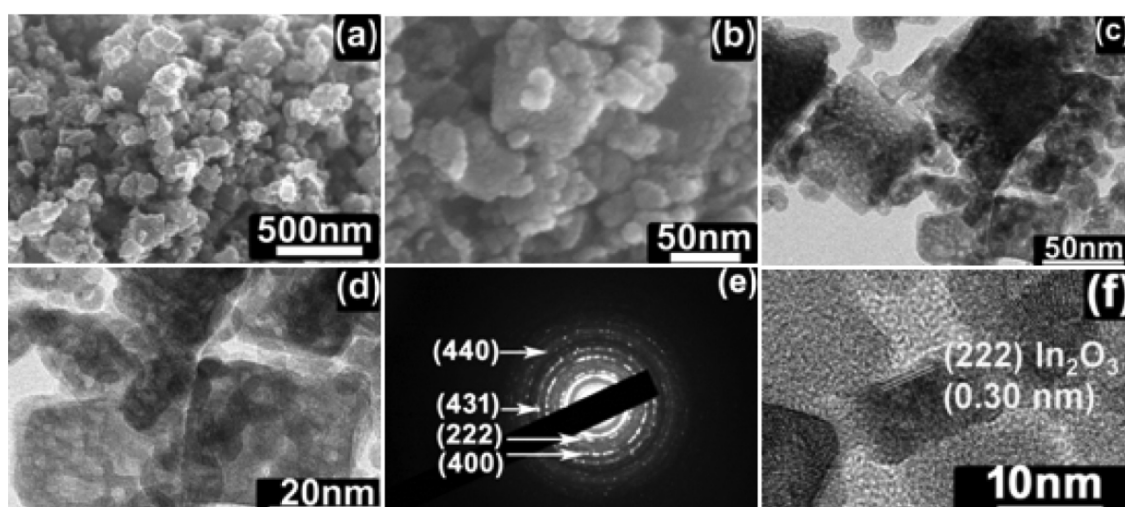

Figure 2. Electron microscopy images of the as-prepared In_2O_3 nanocubes in scanning and transmission modes. (a, b) FESEM images of the as-prepared In_2O_3 nanocubes at two different magnifications; representative TEM images of the In_2O_3 nanocubes at (c) low and (d) higher magnification; (e, f) corresponding SAED pattern and HR-TEM image of the In_2O_3 nanocubes.

Preparation of Mesoporous Indium Oxide (In_2O_3) Nanocubes. The presynthesized $In(OH)_3$ precursor was loaded into a alumina boat, heated to 400 °C at a heating rate of 10 °C/min in a conventional furnace, and calcined at that temperature for 3 h to obtain the In_2O_3 powder.

Preparation of Nitrogen-Doped Reduced Graphene Oxide−Indium Oxide Nanocube (In_{NrGO}) Composites. First, graphene oxide (GO) was synthesized by a modified Hummers's method,[34] as described briefly in the Supporting Information. The preparation of In_{NrGO} composites is represented in Scheme 1. Calculated amounts of the resulting GO and In_2O_3 nanocubes were ultrasonically dispersed in 30 mL of water followed by the addition of 3 mL of 1:1 hydrazine hydrate/aqueous ammonia. The resulting mixture was poured into an autoclave and heated at 180 °C for 12 h. Subsequently, the collected products were purified with water, ethanol, and acetone by centrifugation to yield the nitrogen-doped reduced graphene oxide−In_2O_3 nanocube composites.

Preparation of Reduced Graphene Oxide−Indium Oxide Nanocube (In_{rGO}) Composites. In a typical synthesis, calculated amounts of GO and In_2O_3 nanocubes were ultrasonically dispersed in 30 mL of 1:1 water/ethanol. The final mixture was poured into an autoclave and heated at 180 °C for 12 h. Subsequently, the product

was isolated using a method similar to that discussed for the previous hybrids.

RESULTS AND DISCUSSION

The morphologies of the as-prepared materials were investigated by field-emission scanning electron microscopy (FESEM) and transmission electron microscopy (TEM). Figure 1 shows the electron micrographs of the $In(OH)_3$ nanocubes prepared by a typical hydrothermal reaction. The low-magnification FESEM image (Figure 1a) clearly shows numerous nanocubes of two different sizes with mean diameters of ∼200 and ∼20 nm. The high surface roughness of the nanocubes is clearly demonstrated in the higher-magnification image (Figure 1b), illustrating the porous structure of the material. The TEM image (Figure 1c) clearly shows the cubic morphology of most of the particles. The higher-magnification image (Figure 1d) reveals well-faceted nanocubes with sharp edges. The TEM particle size distribution analysis indicates that more than 80% of the as-synthesized
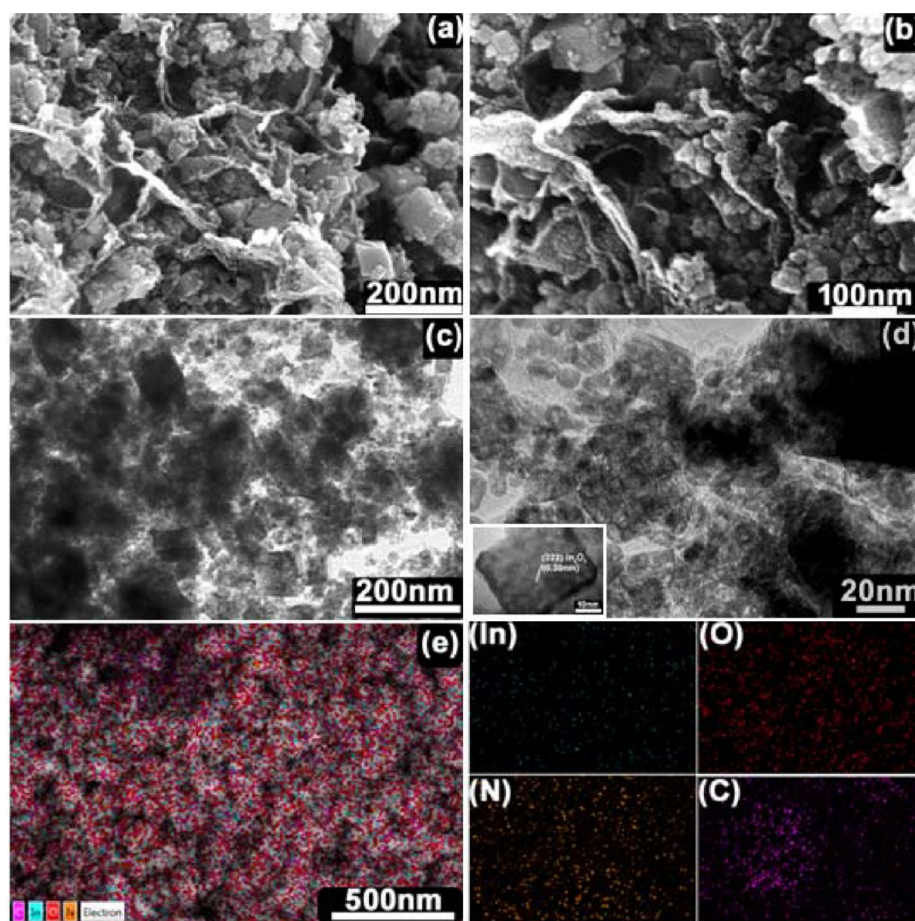
Figure 3. Electron micrographs of the as-prepared In_{NrGO-3} composites. Representative (a, b) FESEM and (c, d) TEM images at different magnifications; inset of panel d: HR-TEM of the In_{NrGO-3} hybrid; (e) the corresponding In, O, N, and C elemental mapping images.

$In(OH)_3$ particles are cubic in shape of size $\sim$20 nm, as measured for 250 cubes. In addition to smaller nanocubes, $\sim$20 nm in size, the as-prepared $In(OH)_3$ contained some larger nanocubes, $\sim$200 nm in size. The higher-magnification TEM image (Figure 1e) reveals the porosity of the material. The electron-dense and electron-depleted regions demonstrate the mesoporous nature of the materials. The inset of Figure 1f is the selected area electron diffraction (SAED) pattern, which confirms the polycrystalline nature of the obtained material. The diffraction rings are attributed to the (200), (220), (222), and (400) planes of the body centered cubic (bcc)-$In(OH)_3$ structure. Similarly, the high-resolution (HR)-TEM micrograph (Figure 1f) exhibits a lattice plane spacing of $\sim$0.397 nm, which corresponds to the (200) plane of bcc-$In(OH)_3$.[35]

Figure 2 shows the electron micrographs of the In_2O_3 nanocubes. As illustrated in the FESEM images (Figure 2a,b), the In_2O_3 nanocubes appreciably retained the parent morphology of $In(OH)_3$. The TEM images (Figure 2c,d) show the high degree of surface roughness and mesoporosity of the In_2O_3 nanocubes compared with the parent $In(OH)_3$ nanocubes. This is due to the removal and dehydration of the capping agents and other residual organic impurities from the surface of the materials during calcination. The SAED patterns (Figure 2e) correspond to the (222), (400), (431), and (440) planes of the bcc-In_2O_3. The HR-TEM image exhibits a d-spacing of 0.30 nm, attributed to the (222) lattice planes of the bcc-In_2O_3.[36,37]

A detailed morphological evaluation of In_{NrGO} (Figure 3) confirms the structure of the as-prepared composites. Figure 3a presents the FESEM image of the In_{NrGO-3} hybrid, illustrating that the In_2O_3 nanocubes are successfully incorporated into the NrGO nanosheets. Furthermore, the crumpled graphene sheets showed many folds and wrinkles and contained several In_2O_3 nanocubes, as observed in the higher-magnification image (Figure 3b). As observed in the FESEM images, a slight structural modification of the In_2O_3 nanocubes occurred during the reduction of GO, when the obtained In_2O_3 nanocubes were ultrasonically dispersed in water along with GO and reduced through a hydrothermal reaction. The high pressure and temperature induce a small structural irregularity in the In_2O_3 nanocubes. The TEM image clearly shows several In_2O_3 nanocubes located on the surface of the two-dimensional NrGO nanosheets (Figure 3c,d). The observed lattice spacing ($\sim$0.30 nm) of In_{NrGO-3} (inset of Figure 3d) corresponds to the (222) plane of the bcc-In_2O_3. The HR-TEM images of pristine NrGO are provided in the Supporting Information (Figure S1) with corresponding discussion. The elemental mapping image (Figure 3e) further reiterates the homogeneous presence of indium, oxygen, carbon, and nitrogen in the In_{NrGO-3} hybrid. The corresponding energy dispersive analysis spectra (Figure S6) show that the atomic percentage of nitrogen is $\sim$5.38% in the composites.

Furthermore, the chemical compositions of the as-prepared materials were investigated by X-ray photoelectron spectroscopy (XPS) analysis. The XPS survey spectrum (Figure S7)
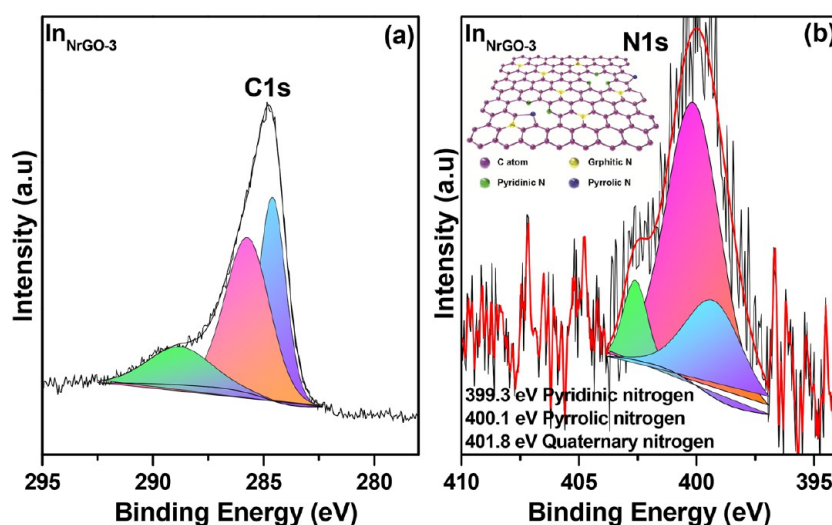
Figure 4. High-resolution (a) C 1s and (b) N 1s core-level X-ray photoelectron spectra of the as-prepared In_{NrGO-3} composite.

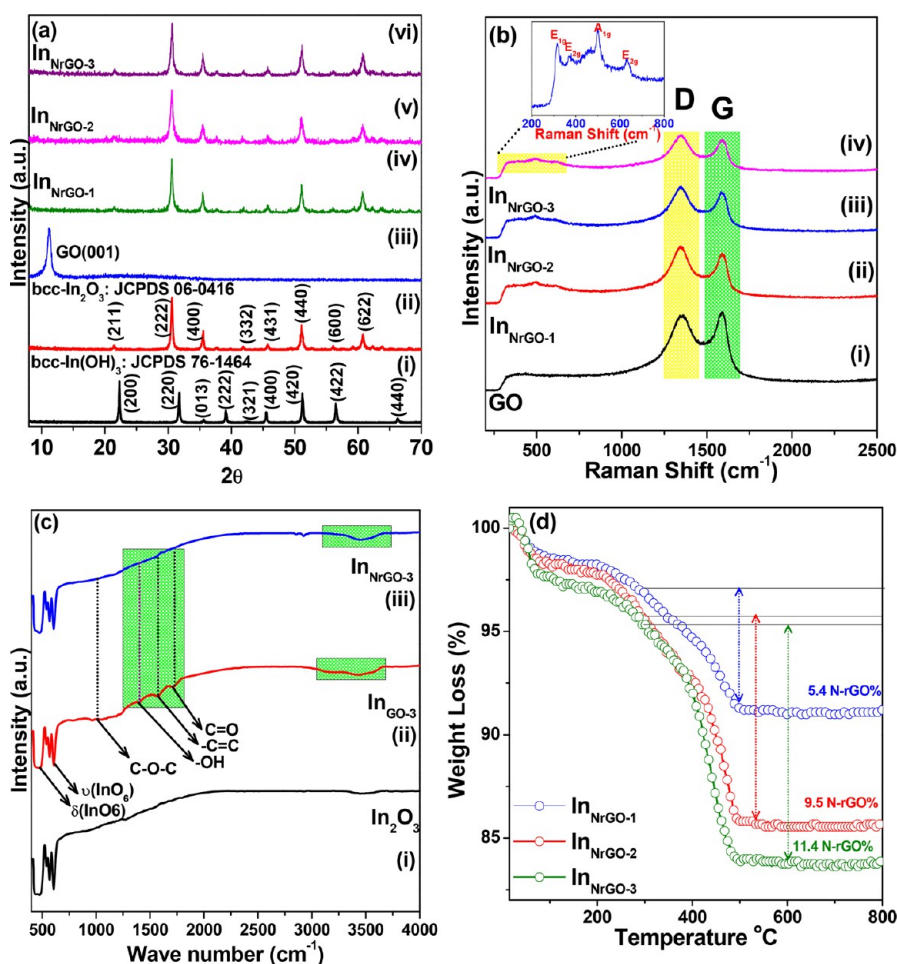**Figure 5.** (a) Powder X-ray diffraction pattern of (i) as-prepared $In(OH)_3$ nanocubes, (ii) In_2O_3 nanocubes, (iii) as-prepared graphene oxide, and (iv–vi) different weight percentage nitrogen-doped reduced graphene oxide nanosheets–In_2O_3 nanocube composites; (b) micro-Raman spectra of (i) as-prepared graphene oxide and (ii–iv) different weight percentage nitrogen-doped reduced graphene oxide-In_2O_3 nanocube composites (inset: micro-Raman spectra of In_2O_3 nanocubes); (c) Fourier transform infrared spectra of the as-prepared (i) In_2O_3, (ii) In_{GO-3}, and (iii) In_{NrGO-3} composites; (d) thermogravimetric analysis of the as-prepared In_{NrGO} samples. Each sample was heated from room temperature to 800 °C at a scan rate of 10 °C/min.

clearly shows the photoelectron peaks of indium, oxygen, nitrogen, and carbon. Figure 4 shows the core-level spectra of In_{NrGO-3} in the carbon and nitrogen regions. The carbon peak

(Figure 4a) is deconvoluted into three peaks. The peak at 284.60 eV corresponds to sp^2 C atoms bound to N; other one at 285.8 eV originates from the hydroxyl and epoxy carbons.

The peak at ~288.9 eV corresponds to the carboxylic carbon bond.[38] The core-level high-resolution XPS spectrum in the N 1s region, shown in Figure 4b, is deconvoluted into three peaks, where the peaks observed at 399.3 and 400.1 eV correspond to the pyridinic and pyrrolic N, while the peak at 401.7 eV is ascribed to quaternary N.[39,40] The inset in Figure 4b represents the different forms of nitrogen doped into graphene. Table S1 shows the atomic percentages of nitrogen, carbon, oxygen, and indium in the In_{NrGO-3} hybrids. The chemical reduction of graphene oxide under hydrothermal conditions with the introduction of N (2.35 at%) by hydrazine and ammonia into graphene led to the successful doping of nitrogen.

The crystal structure of the obtained materials was determined by X-ray diffraction (XRD) (Figure 5a) analysis. The diffraction peaks in Figure 5a(i) could be indexed to the bcc-$In(OH)_3$ with lattice parameter a = 0.7972 nm, which is consistent with previous reports.[41] The highest-intensity peak corresponding to the (200) plane indicates that the $In(OH)_3$ nanocubes grow along the [100] direction. Figure 5a(ii) displays the diffraction pattern of In_2O_3 obtained by the calcination of as-prepared $In(OH)_3$. The diffraction peaks correspond to the bcc-In_2O_3 with lattice parameter a = 1.002 nm (JCPDS card no.: 71-2195).[42] The diffraction peaks of the GO (Figure 5a(iii)) displays a strong peak at 11.7°, corresponding to the d-spacing (d_{001}) of 0.75 nm, indicating the hydration and exfoliation of GO.[43] The diffraction patterns of the as-synthesized In_{NrGO} hybrids are illustrated in Figure 5a(iv–vi). The GO diffraction pattern (d_{001}) completely disappears after the hydrothermal reaction, indicating that the ordered crystallographic orientation may have been lost, resulting in random packing of the graphene sheets. The other peaks are indexed to the bcc-In_2O_3. Absence of other impurity phases unambiguously establishes the formation of phase-pure In_{NrGO} composites.

Figure 5b represents the Raman spectra of the obtained materials. The Raman bands observed at 360 (E_{2g}), 490 (A_{1g}), and 624 (E_{2g}) cm^{-1} (inset in Figure 5b) correspond to the optical phonons associated with the bcc crystal structure of In_2O_3.[44] The peaks at 490, 631, and 308 cm^{-1} correspond to the stretching $\nu(InO_6)$ and bending $\delta(InO_6)$ vibration of the InO_6 octahedra, respectively. The band at 360 cm^{-1} could be indexed to the stretching vibration of the indium–oxygen–indium plane.[44] The Raman spectra of the obtained GO and In_{NrGO} composites (Figure 5b(i–iv)) show two prominent peaks located at 1345 and 1587 cm^{-1} originating from the well-defined D and G bands.[45] The defects in the graphitic structures are usually determined by the peak intensity ratio of the D and G bands (I_D/I_G). The I_D/I_G values of GO, In_{NrGO-1}, In_{NrGO-2}, and In_{NrGO-3} are 0.982, 1.0425, 1.0442, and 1.0478, respectively. The increase in I_D/I_G clearly indicates that graphene oxide is reduced in the In_{NrGO} sample, resulting in the formation of more disordered and defective carbon materials during hydrothermal synthesis.[46]

Figure 5c shows the Fourier transform infrared (FTIR) spectrum of the obtained materials. The bands located at lower wavenumbers correspond to the fundamental overtones of In_2O_3 (Figure 5c(i)). The strong absorptions at 420 and ~620 cm^{-1} are assigned to the stretching and bending vibrations of In_2O_3.[47,48] The FTIR spectrum (Figure 5c(ii)) of indium oxide–graphene oxide (In_{GO-3}) clearly shows the strongest absorption bands, which originate from the vibrational bands of several oxygen containing functionalities such as >C=O/COOH (1713 cm^{-1}), epoxy (1032 cm^{-1}), C–OH (1151

cm^{-1}), and –OH (3442 cm^{-1}). These bands do not appear in the FTIR spectrum of the In_{NrGO-3} composite (Figure 5c(iii)), indicating that graphene oxide is completely reduced.[38]

Furthermore, thermogravimetric analysis (TGA) was performed to identify the thermal stabilities and compositions of the as-prepared In_{NrGO} materials (Figure 5d). The TGA/DTA profile of the obtained $In(OH)_3$ shows (Figure S12) a three-step mass loss. The initial mass reduction below 200 °C attributed to the eviction of OH and bound H_2O molecules. The mass reduction between 200 and 300 °C corresponds to the eviction of organic molecules that were used during synthesis. The final mass loss between 300 and 400 °C corresponds to the phase transformation of $In(OH)_3$ to In_2O_3. Overall, the 20% mass reduction observed during the phase transformation process is consistent with previous reports.[49] As observed in Figure 5d, the TGA curves of all the In_{NrGO} materials show a two-step mass loss. The preliminary mass loss below 300 °C is mostly attributed to the removal of trapped H_2O and other organic molecules. The subsequent mass reduction observed between 300 and 500 °C corresponds to the burning and removal of carbon molecules from the In_{NrGO} composites. Drawing inference from TGA analysis, the approximate calculated weight percentages of NrGO in the In_{NrGO-1}, In_{NrGO-2}, and In_{NrGO-3} composites are ~5.4, 9.5, and 11.4%, respectively.

The surface area of the obtained products was determined by N_2 adsorption–desorption isotherm analysis (Figure 6). All the
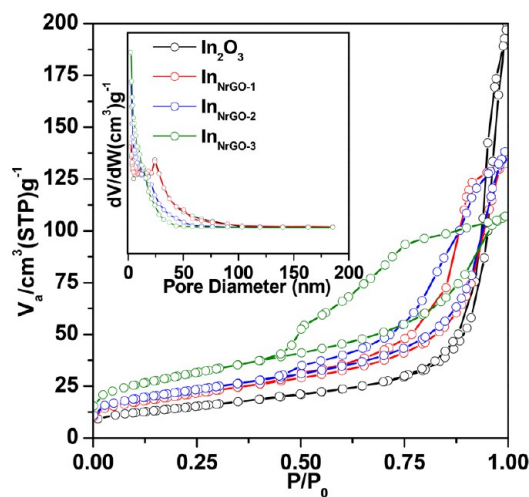

Figure 6. N_2 adsorption–desorption Barrett–Joyner–Halenda (BJH) isotherms of the as-prepared In_2O_3 nanocubes and In_{NrGO} composites. Inset: the corresponding BJH pore size distributions from the adsorption branch.

samples provide a typical IV isotherm with a clear H3-type hysteresis loop. The hysteresis loop, with its relative pressure in the range of 0.3–0.8 and 0.8–1.0, is attributed to the mesopores and macropores of the as-prepared materials.[50,51] The Brunauer–Emmett–Teller surface areas of the In_2O_3 nanocubes, In_{NrGO-1}, In_{NrGO-2}, and In_{NrGO-3} are found to be 71.6, 77.8, 104.9, and 125.2 $m^2 \cdot g^{-1}$, which are appreciably high and beneficial for enhancing the gas-sensing characteristics. The pore size in all the as-prepared samples is around 2–20 nm as seen from the pore size distribution plots in the inset of Figure 6.

Gas-Sensing Characteristics. The fabrication techniques and measurement setup[52] used to characterize the sensors are

briefly described in the Supporting Information. The CO-sensing performance of the developed gas sensors was analyzed in a dry air environment from 35 to 300 °C. The sensors show a maximum sensor response at an elevated temperature, at which the adsorption−desorption kinetics of the gas are optimum. Thus, to determine the elevated sensing temperature, the sensing characteristics of In_2O_3 and the In_{NrGO} composites to 100 ppm of CO were studied as a function of temperature (RT < T_s < 300 °C). Figure 7a shows the sensing characteristics
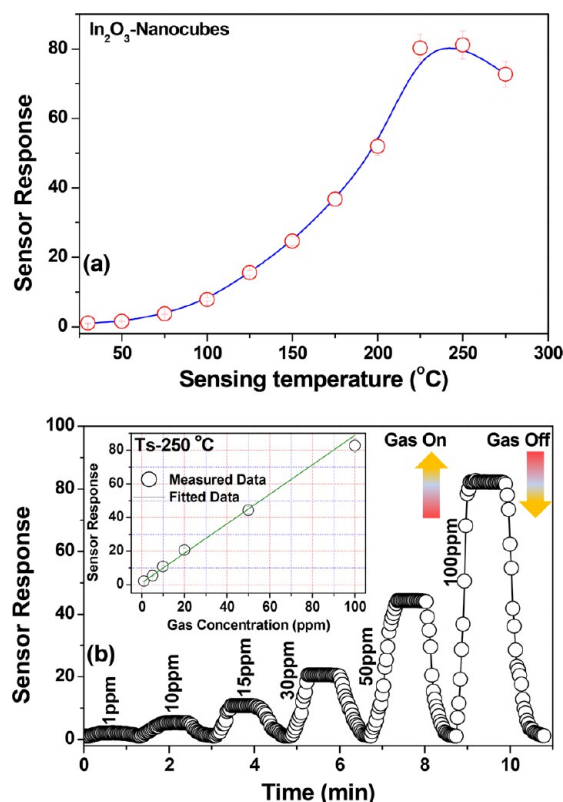
strates that the sensor shows a wide detection limit with a sensor response of $S_R \sim 3.7$ for 1 ppm of CO and $S_R \sim 82.6$ for 100 ppm of CO. The CO response (Γ_{RES}) and recovery time (Γ_{REC}) for the In_2O_3 nanocube sensor (Figure S13) to 100 ppm are estimated to be $\Gamma_{RES} \sim 16$ s and $\Gamma_{REC} \sim 29$ s, whereas the Γ_{RES} and Γ_{REC} of the sensor to 1 ppm are ~21 s and ~14 s, respectively.

Furthermore, to effectively enhance the sensing characteristics, In_2O_3 nanocubes were incorporated into nitrogen-doped reduced graphene oxide. Figure 8 shows the temperature-

Figure 7. (a) Sensing responses of the as-prepared In_2O_3 nanocubes to 100 ppm of CO as a function of the sensing temperature; (b) dynamic sensing response of the as-prepared In_2O_3 nanocubes as a function of the gas concentration at a sensing temperature (T_s) of 250 °C. Inset: linear fitting curve of the sensing response of In_2O_3 nanocubes toward different concentrations of CO.
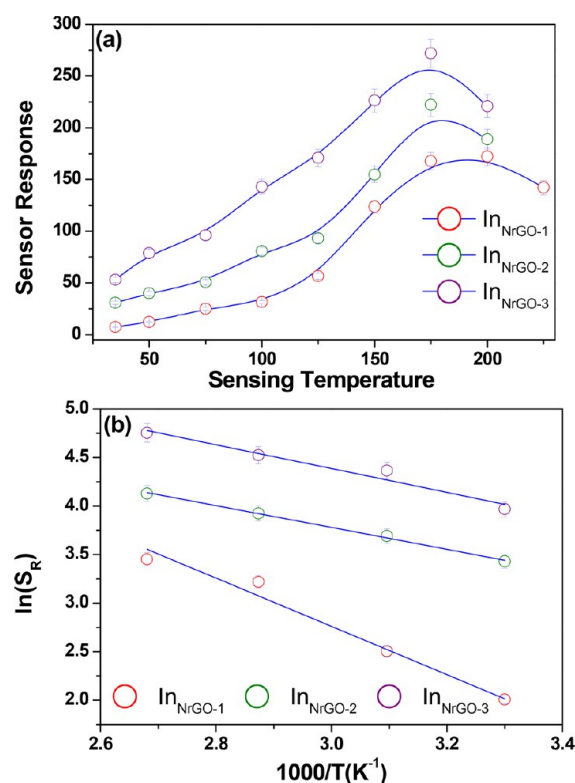

Figure 8. (a) Sensing response of sensors based on the In_{NrGO} composites to 100 ppm of CO as a function of the sensing temperature; (b) corresponding Arrhenius plots.

of the as-prepared In_2O_3 nanocubes to 100 ppm of CO. The temperature-dependent sensing studies show that the rate of CO adsorption increases with increasing sensing temperature up to an optimum operating temperature. The as-prepared In_2O_3 nanocube sample shows the highest response of $S_R \sim 82$ at 250 °C. The sensing result suggests that the highest sensitivity of the as-prepared In_2O_3 nanocubes at lower temperature is attributed to the large surface-to-volume ratio and hierarchical mesoporous nature of the material. The large surface area and the porosity of the as-prepared In_2O_3 nanocubes provide additional advantages by increasing the effective reaction sites for the surface chemisorption of the CO.

To investigate the maximum detection limit of the as-prepared In_2O_3 nanocubes, additional CO-sensing analyses were performed at 250 °C as a function of the gas concentration (1 ppm < G_C < 100 ppm). As shown in Figure 7b, the sensor response improves with increasing CO concentration. The dynamic sensor response clearly demon-

dependent sensing characteristics of sensors based on the In_{NrGO} composites to 100 ppm of CO. As observed from the sensing characteristics (Figure 8a), the sensors constructed with the In_{NrGO} composites exhibited improved sensing performance over those composed of pristine In_2O_3 nanocubes. The sensor based on the In_{NrGO-3} composite shows a maximum sensing response of ~273 at 175 °C, whereas the sensor responses of In_{NrGO-2} and In_{NrGO-1} are $S_R \sim 222$ at 175 °C and $S_R \sim 170$ at 200 °C, respectively. The sensors based on the In_{NrGO} composites also showed detectable sensing responses close to ambient temperatures (35 °C). The sensor response of the In_{NrGO-3} composite at room temperature is ~53.4, while those of In_{NrGO-2} and In_{NrGO-1} are ~35.4 and ~8.3, respectively. The Arrhenius plots of the sensing responses (Figure 8b) to 100 ppm of CO, shows a strong linear dependence of the sensor responses on the sensing temperature. From the Arrhenius plots, the sensor responses of In_{NrGO-1}, In_{NrGO-2}, and In_{NrGO-3} at room temperature are found to be $\ln(S_R) \sim 1.9$, 3.42, and 4.03, respectively. The activation energies of the In_{NrGO-1}, In_{NrGO-2}, and In_{NrGO-3} sensing materials were calculated from the Arrhenius plots of the sensor response and were found to be
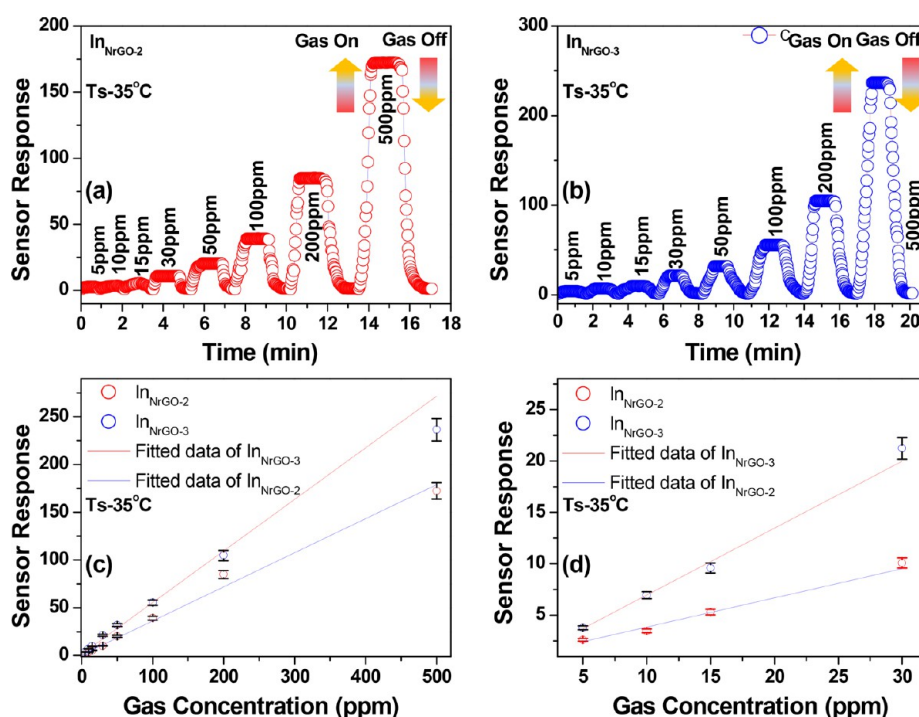
Figure 9. Dynamic sensor responses of sensors fabricated with (a) In_{NrGO-2}; (b) In_{NrGO-3} composites to different concentrations of CO at an operating temperature of ~35 °C, as a function of time; (c, d) linear fitting curve of the sensing response of In_{NrGO-2} and In_{NrGO-3} composites toward different concentrations of CO.

~0.21, 0.096, and 0.064 eV. The lower activation energy of In_{NrGO-3} compared to that of In_{NrGO-1} and In_{NrGO-2} signifies the higher sensing response of the material.

To effectively compare the effect of nitrogen doping, further CO-sensing analyses were performed on pristine rGO-incorporated In_2O_3 nanocubes (In_{rGO}). The temperature-dependent sensing characteristics of the In_{rGO} composite are provided in Figure S14. The sensor responses of the In_{rGO-1}, In_{rGO-2}, and In_{rGO-3} composites are found to be ~128, 159, and 197 at 200 °C; meanwhile, the sensor responses at room temperature are significantly lower at ~1.6, 6.6, and 15.2, respectively. The bar plot in Figure S15 depicts a comparison of the sensor responses of all the fabricated gas sensors. Among the various sensors, the one based on the In_{NrGO-3} composite shows the best sensor response at all operating temperatures.

The dynamic sensor responses of the In_{NrGO-2} and In_{NrGO-3} composites to different concentrations of CO (500, 200, 100, 50, 30, 15, 10, and 5 ppm) were further investigated at 35 °C to determine their maximum sensitivity limit. As observed in Figure 9, the sensor response improves dramatically with increasing CO concentration. Although the dynamic sensing studies unambiguously demonstrate that sensors based on both the In_{NrGO-2} and In_{NrGO-3} composites exhibit excellent sensing characteristics of CO at 35 °C, the In_{NrGO-3} sensor exhibited a maximum sensitivity greater than that of the In_{NrGO-2} sensor. Both sensors can sense CO as low as 5 ppm at ambient temperatures, indicating their broad linear range and wide detection limits. The response (Γ_{RES}) and recovery (Γ_{REC}) times of the In_{NrGO-2} and In_{NrGO-3} sensors at room temperature to 500 and 5 ppm of CO are shown in Figure S16. The Γ_{RES} and Γ_{REC} of the In_{NrGO-2} sensor to 500 ppm ($S_R \sim 172$) are estimated to be ~36 s and ~46 s, whereas the Γ_{RES} and Γ_{REC} of the In_{NrGO-3} sensor to 500 ppm ($S_R \sim 236$) are ~48 s and ~52 s. The Γ_{RES} and Γ_{REC} of each of these sensors to 5 ppm of CO

are found to be ~16 s and ~32 s for In_{NrGO-2} ($S_R \sim 2.6$) and $\Gamma_{RES} \sim 22$ s and $\Gamma_{REC} \sim 32$ s for In_{NrGO-3} ($S_R \sim 3.7$).

The long-term stability of the In_{NrGO-2} and In_{NrGO-3} sensors was investigated at 35 °C to 100 ppm of CO for 50 days. As shown in Figure S17, the sensor responses even at the 50th day show only very small depreciation, indicating the high stability of the sensors. The influence of humidity on the In_{NrGO-3} sensor performance was probed (Figure S18) in dry nitrogen and ambient air with a controlled relative humidity (RH 55%). The sensing responses of the sensor to 100 ppm of CO in dry nitrogen and ambient air at room temperature are found to be $S_R \sim 53$ and $S_R \sim 54$, respectively, indicating that the sensor is insensitive to humidity. Furthermore, the selectivity of the In_{NrGO-3} sensor was investigated at 35 °C to 20 ppm of CO and other interfering gases. As observed in Figure 10 the sensor shows the maximum response ($S_R \sim 11$) to CO, which is ~4.2, 3.5, 4, 5, 7.5, 4.2, and 9 times higher than its responses to hydrogen sulfide, ammonia, ethanol, methanol, hydrogen, acetone vapors, and RH 50% H_2O, respectively, indicating its high selectivity to CO. The gas-sensing studies conclude that the $In_{N-rGO-3}$ composite is the optimized material with the maximum CO-sensing response ($S_R \sim 53.4$ at 35 °C and $S_R \sim 273$ at 175 °C). To demonstrate the improved performance of the In_{NrGO-3} sensor, we compared the CO-sensing performance of our device with those of various reported CO sensors (Table 1).

Plausible Gas-Sensing Mechanism. The gas-sensing characteristics establish that incorporating NrGO with In_2O_3 nanocubes has been successful in improving the CO-sensing characteristics of pristine In_2O_3. The high sensitivity of the proposed CO sensor is attributed to (i) the large surface-to-volume ratio and hierarchical mesoporous structure of the In_2O_3 nanocubes, (ii) electric effects induced by the heterojunction between NrGO and the In_2O_3 nanocubes, (iii)
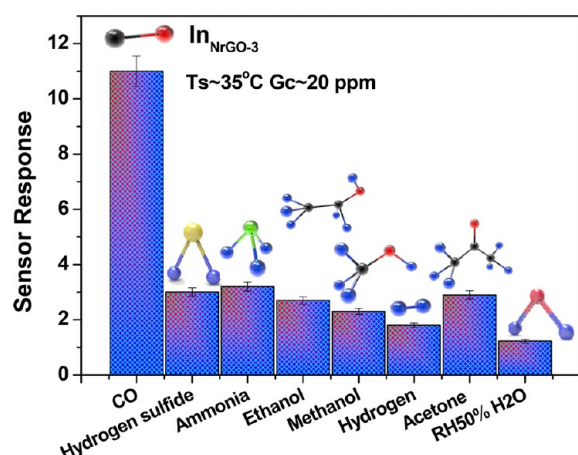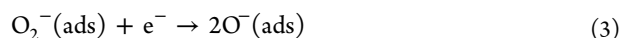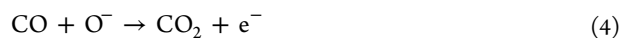
Figure 10. Bar plot depicting the sensor responses and selectivity of the In_{NrGO-3} composite to 20 ppm of CO, hydrogen sulfide, ammonia, ethanol, methanol, hydrogen, acetone vapors, and RH 50% H_2O at 35 °C.

the spillover effect induced by nitrogen-doped reduced graphene oxide, and (iv) electrical conductivity effects of the NrGO network. To further understand the exact sensing mechanism of the In_{NrGO} hybrids, we first describe the sensing principle of pristine In_2O_3.

The most commonly accepted gas-sensing theory for n-type materials like indium oxide is that at elevated operating temperature, the surface adsorbed O_2 molecules are ionized by accepting electrons from the semiconducting oxide and form oxygen radicals. The specific reactions are as follows:[60]

$$O_2(gas) \rightarrow O_2(ads) \quad (1)$$

$$O_2(ads) + e^- \rightarrow O_2^-(ads) \quad (2)$$

$$O_2^-(ads) + e^- \rightarrow 2O^-(ads) \quad (3)$$

Upon exposure to a reducing gas such as CO, a chemical reaction is initiated whereby the ionized oxygen releases electrons thereby increasing the electrical conductivity (σ) of the sensor. The chemical reaction paths are as follows:[61]

$$CO + O^- \rightarrow CO_2 + e^- \quad (4)$$

$$2CO(gas) + O_2^-(ads) \rightarrow 2CO_2(gas) \quad (5)$$

Although the chemisorption–desorption of oxygen radicals is the influencing factor of the sensing characteristics, the amount of surface-adsorbed and desorbed oxygen species that can

actually participate in gas sensing is strongly dependent on the sensing material. As observed from the sensing results, pristine In_2O_3 nanocubes can detect CO concentrations as low as 1 ppm at 250 °C. The enhanced sensitivity is attributed to two key features of the material. First, the surface of the In_2O_3 nanocubes is more reactive owing to its high surface area ($\sim$72 m^2/g). The highly reactive sites of the In_2O_3 nanocubes adsorb more oxygen molecules and form a high density of ionized oxygen species. Second, an important factor is the hierarchical and porous structure of the materials. The high porosity and large accessible surface area provide numerous pathways for the diffusion of CO gas molecules, thereby reducing the gas diffusion distance, increasing the gas diffusion rate, and enhancing the kinetics of surface gas adsorption and desorption.

The incorporation of catalytic material into metal oxide sensors can effectively enhance the room-temperature sensing response and selectivity of the sensor. The reason is that metal oxides are unable to generate a substantial volume of oxygen species at ambient temperatures. As discussed earlier, the chemisorption of the oxygen species is influenced by the operating temperature and the surface characteristics of the sensing material.[54,62] The enhanced sensing performance at ambient temperature is attained by the incorporation of In_2O_3 nanocubes into the NrGO matrix. The effect of N doping in rGO can be explained based on two rationales: (i) electronic modification and (ii) chemical functionalization (Figures S19 and S20). The abundance of free-flowing π-electrons renders rGO a potential catalyst; however, these π-electrons are too passive at room temperature. Doping with nitrogen, a comparatively stronger electronegative element than carbon, activates the carbon π-electrons through conjugation with the lone-pair electrons.[63] Furthermore, the electron-gaining capability of the N element generates net positive charges on the neighboring C atoms to promote oxygen adsorption. Thus, the adsorbed O_2 molecules are ionized and form molecular oxygen species (O_2^-) on the positively charged C. These then spill onto the sensor surface through a chemical sensitization process. This explains the decrease in the optimum sensing temperature with the addition of NrGO. N doping into rGO provides additional charge carriers thereby altering the electronic properties of graphene[64] that could be favorable in CO-sensing. As demonstrated by Ma et al., CO molecules can be effectively adsorbed on pyridinic N, accompanied by an ample charge transfer.[30] The nitrogen species also increase the polarizability of CO and the rate of CO dissociation, both of which lead to an enhanced sensor response.

Table 1. CO-Sensing Performance of the Proposed Sensor and That of Other Published CO Sensors[a]

material	T_s (°C)	S_R	G_C (ppm)	Γ_{RES} (s)	Γ_{REC} (s)	ref.
Pt–In_2O_3; Pd–In_2O_3	RT	50	$\sim$2.8–7.2	50	60	Lai and Chen[53]
Au nanoparticle-In_2O_3	RT	104	200–5	130	50	Singh et al.[54]
Au/SnO_2	RT	N/A	500	20	200	Manjula et al.[3]
CNT/Au/SnO_2 nanotubes	RT	70	500–2500	<20	N/A	Du et al.[55]
Co_3O_4/PEI-CNTs	RT	30.3	5–1000	8	30	Dang et al.[56]
Au/ZnO nanowires	RT	5	100	N/A	N/A	Joshi et al.[57]
ZnO/Au nanostars	RT	55.5	500–50	41–10	40–12	Arunkumar et al.[52]
CoOOH	RT	5	50	20	20	Geng et al.[58]
RGO/Au/SnO_2	RT	20.3	2	180	199	Kim et al.[59]
In_2O_3–N-rGO	RT	4.4 ± 5%	5	22	32	this work

[a]T_S, sensing temperature; RT, room temperature; S_R, sensor response; G_C, gas concentration; Γ_{RES}, response time; Γ_{REC}, recovery time.

Scheme 2. (a) Representative Physical Models and (b) Energy Band Diagrams Depicting the CO-Sensing Mechanism in Air and CO Environments
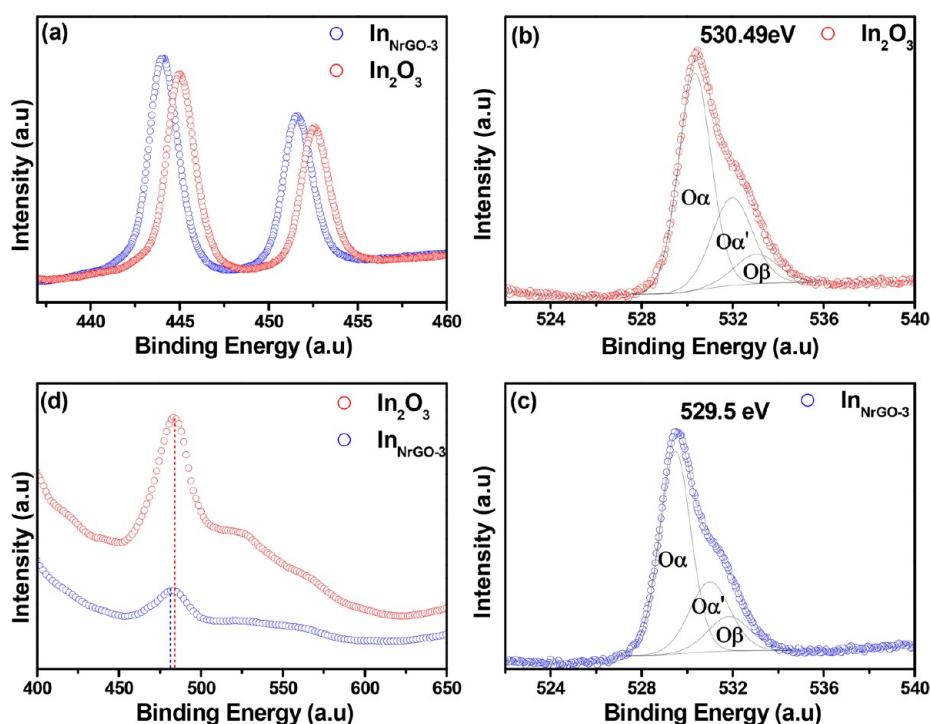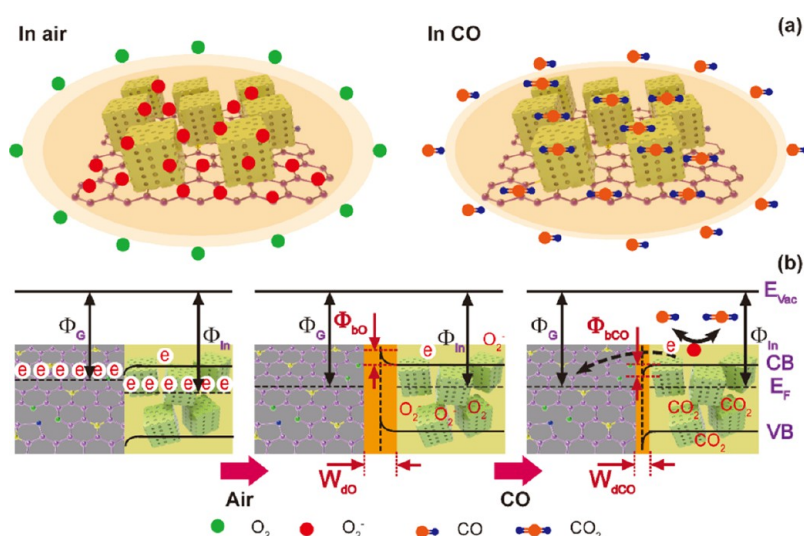

Figure 11. High-resolution core-level X-ray photoelectron spectra of the as-prepared In_2O_3 nanocubes and In_{NrGO-3} composites in the (a) indium and (b, c) oxygen regions; (d) photoluminescence spectra of the In_2O_3 nanocubes and In_{NrGO-3} hybrids.

In an alternative proposition, the enhanced CO-sensing response of In_{NrGO} at ambient temperature could be explained based on the formation of the N-graphene–In_2O_3 heterojunction and an active interface between N-graphene–In_2O_3 nanocubes, as represented in Scheme 2. The In_2O_3 nanocubes are uniformly distributed on the N-graphene sheets, and heterojunctions are regularly formed in the In_{NrGO} composites. Before the chemisorption of oxygen species from air, the heterojunction between NrGO–In_2O_3 would be ohmic because the work function of each material is different ($\Phi_G < \Phi_{In}$). Hence, some electrons are accumulated on the surface of the In_2O_3 nanocubes to align the Fermi level positions. Subsequently, the electrons are shifted to the chemisorbed

O_2 species (Scheme 2b), generating the depletion region at the heterojunction, with a width W_{dO} and barrier height Φ_{bO}, causing a decrease in the electrical conductivity of the sensing material.

This can be explained based on the X-ray photoelectron spectra and photoluminescence (PL) spectra of the In_2O_3 nanocubes and In_{NrGO-3} hybrids (Figure 11). The core-level spectra of the In_2O_3 nanocubes and In_{NrGO-3} hybrids (Figure 11a) show the characteristic doublet of In $3d_{3/2}$ and In $3d_{5/2}$ at ~444.18 and 451.9 eV. As observed, the band position of the characteristic doublets of In^{3+} in the In_{NrGO-3} composite shifts to lower binding energy by ~0.7 eV, indicating the strong chemical and electronic interaction between NrGO and In_2O_3.

The O 1s core-level spectra of In$_2$O$_3$ and In$_{NrGO-3}$ are shown in Figure 11b,c, which are deconvoluted into three sub-bands depending on their different properties, denoted as Oα, Oα', and Oβ. As shown, the O 1s binding energy of the In$_{NrGO-3}$ nanocomposite is lower than that of the pristine In$_2$O$_3$ nanocubesby almost 1 eV, further indicating the strong electronic interaction between In$_2$O$_3$ and NrGO. This observation also illustrates that the heterojunction of In$_2$O$_3$ and NrGO enhances the adsorption of oxygen species at the interface, even at lower temperatures. The PL spectrum (Figure 11d) of the In$_{NrGO-3}$ hybrid exhibits a slight blue shift and has a much lower intensity compared to that of pristine In$_2$O$_3$ nanocubes. This suggests that the NrGO nanosheets serve as electron acceptors, thereby quenching the PL of In$_2$O$_3$ nanocubes by decreasing radiative recombination.[65] On the basis of these observations, we propose the key mechanism underlying the synergetic effect of the In$_2$O$_3$ nanocubes and NrGO. The heterojunctions between In$_2$O$_3$ and NrGO act as electron migration paths that accelerate the sensor response during gas sensing.

In a CO environment, the dissociated CO species can preferentially and strongly adsorb at graphene−metal oxide interfaces because these interfaces present several active sites, like vacancies, line defects, and strong electronic interactions between graphene and the metal oxides.[66,67] The CO adsorbed at the interfaces of N-graphene−In$_2$O$_3$ nanocubes reacts with molecular oxygen species as described in eqs 4 and 5, leading to the electron transfer to the conduction band of the In$_2$O$_3$ nanocubes. Under these circumstances, the NrGO nanosheets receive electrons from the adjacent In$_2$O$_3$ nanocubes, which act as electron transporters. This results in an extensive decrease in the depletion width and potential barrier height, as depicted in the energy band model (Scheme 2). All these features of the In$_{NrGO}$ composites manifest together, leading to enhanced CO sensing at room temperature.

CONCLUSION

Hierarchical In$_2$O$_3$ nanocubes and composites of NrGO and In$_2$O$_3$ nanocubes were successfully prepared via a facile hydrothermal route. The findings from different characterization techniques were consistent. N$_2$ adsorption−desorption isotherm analysis revealed the high surface area of the materials. The as-synthesized materials were systematically investigated for CO sensing at different sensing temperatures. The gas-sensing studies revealed that NrGO incorporation into In$_2$O$_3$ led to a dramatic improvement in the sensing response to 100 ppm of CO from $S_R \sim 82$ at 250 °C to $S_R \sim 273$ at 175 °C. The incorporation of NrGO not only increased the sensor response but also effectively reduced the sensing temperature. The In$_{NrGO-2}$ and In$_{NrGO-3}$ sensors showed a wide detection limit and a maximum sensitivity limit as low as 5 ppm at ∼35 °C. Furthermore, the sensor also showed an excellent selectivity toward CO against hydrogen sulfide, ethanol, methanol, ammonia, hydrogen, acetone vapors, and RH 50% H$_2$O. The enhanced sensing performance of In$_{NrGO}$ hybrids at ambient temperature is attributed to the 3D porous structure and high surface area of the In$_2$O$_3$ nanocubes along with the excellent gas adsorption and superb charge-transport capabilities of NrGO.

ASSOCIATED CONTENT

Supporting Information

The Supporting Information is available free of charge on the ACS Publications website at DOI: 10.1021/acsami.7b06253.

Preparation of graphene oxide; details of the analytical techniques; supporting figures and table as described in the text (PDF)

AUTHOR INFORMATION

Corresponding Author
*Tel.: +82 62 530 1684. E-mail: mems@jnu.ac.kr.

ORCID
Dong Weon Lee: 0000-0002-6624-6949

Notes
The authors declare no competing financial interest.

ACKNOWLEDGMENTS

REFERENCES

(1) Pijolat, C.; Pupier, C.; Sauvan, M.; Tournier, G.; Lalauze, R. Gas Detection for Automotive Pollution Control. *Sens. Actuators, B* **1999**, 59, 195−202.

(2) Kamionka, M.; Breuil, P.; Pijolat, C. Atmospheric Pollution Measurement with a Multi-materials Sensing Device. *Mater. Sci. Eng., C* **2006**, 26, 290−296.

(3) Manjula, P.; Arunkumar, S.; Manorama, S. V. Au/SnO$_2$ an Excellent Material for Room Temperature Carbon Monoxide Sensing. *Sens. Actuators, B* **2011**, 152, 168−175.

(4) Zhang, T.; Liu, L.; Qi, Q.; Li, S.; Lu, G. Development of Microstructure In/Pd-doped SnO$_2$ Sensor for Low-level CO Detection. *Sens. Actuators, B* **2009**, 139, 287−291.

(5) Xiang, Q.; Meng, G. F.; Zhao, H. B.; Zhang, Y.; Li, H.; Ma, W. J.; Xu, J. Q. Au Nanoparticle Modified WO$_3$ Nanorods with Their Enhanced Properties for Photocatalysis and Gas Sensing. *J. Phys. Chem. C* **2010**, 114, 2049−2055.

(6) Wang, Y.; Cao, J.; Wang, S.; Guo, X.; Zhang, J.; Xia, H.; Zhang, S.; Wu, S. Facile Synthesis of Porous α-Fe$_2$O$_3$ Nanorods and Their Application in Ethanol Sensors. *J. Phys. Chem. C* **2008**, 112, 17804− 17808.

(7) Li, B.; Xie, Y.; Jing, M.; Rong, G.; Tang, Y.; Zhang, G. In$_2$O$_3$ Hollow Microspheres: Synthesis from Designed In(OH)$_3$ Precursors and Applications in Gas Sensors and Photocatalysis. *Langmuir* **2006**, 22, 9380−9385.

(8) Mahendraprabhu, K.; Elumalai, P. Stabilized Zirconia-based Selective NO$_2$ Sensor Using Sol-gel Derived Nb$_2$O$_5$ Sensing-electrode. *Sens. Actuators, B* **2017**, 238, 105−110.

(9) Sett, D.; Basak, D. Highly Enhanced H$_2$ Gas Sensing Characteristics of Co: ZnO Nanorods and its Mechanism. *Sens. Actuators, B* **2017**, 243, 475−483.

(10) Neri, G.; Bonavita, A.; Micali, G.; Rizzo, G.; Callone, E.; Carturan, G. Resistive CO Gas Sensors based on In$_2$O$_3$ and InSnO$_x$ Nanopowders Synthesized via Starch-aided Sol−gel Process for Automotive Applications. *Sens. Actuators, B* **2008**, 132, 224−233.

(11) Lim, S. K.; Hwang, S.-H.; Chang, D.; Kim, S. Preparation of Mesoporous In$_2$O$_3$ Nanofibers by Electrospinning and Their Application as a CO Gas Sensor. *Sens. Actuators, B* **2010**, 149, 28−33.

(12) Shanmugasundaram, A.; Ramireddy, B.; Basak, P.; Manorama, S. V.; Srinath, S. Hierarchical In (OH) $_3$ as a Precursor to Mesoporous In$_2$O$_3$ Nanocubes: a Facile Synthesis Route, Mechanism of Self-assembly, and Enhanced Sensing Response toward Hydrogen. *J. Phys. Chem. C* **2014**, 118, 6909−6921.

(13) Lee, J.-H. Gas Sensors Using Hierarchical and Hollow Oxide Nanostructures: Overview. *Sens. Actuators, B* **2009**, 140, 319−336.

(14) Phani, A. R. X-ray Photoelectron Spectroscopy Studies on Pd Doped SnO$_2$ Liquid Petroleum Gas Sensor. *Appl. Phys. Lett.* **1997**, 71, 2358−2360.

(15) Liu, X.; Zhang, J.; Guo, X.; Wu, S.; Wang, S. Amino Acid-assisted One-pot Assembly of Au, Pt Nanoparticles onto One-dimensional ZnO Microrods. *Nanoscale* **2010**, *2*, 1178−1184.

(16) Zhang, J.; Liu, X.; Guo, X.; Wu, S.; Wang, S. A General Approach to Fabricate Diverse Noble-Metal (Au, Pt, Ag, Pt/Au)/Fe$_2$O$_3$ Hybrid Nanomaterials. *Chem. - Eur. J.* **2010**, *16*, 8108−8116.

(17) Kolmakov, A.; Klenov, D. O.; Lilach, Y.; Stemmer, S.; Moskovits, M. Enhanced Gas Sensing by Individual SnO$_2$ Nanowires and Nanobelts Functionalized with Pd Catalyst Particles. *Nano Lett.* **2005**, *5*, 667−673.

(18) Vander Wal, R. L.; Hunter, G. W.; Xu, J. C.; Kulis, M. J.; Berger, G. M.; Ticich, T. M. Metal-oxide Nanostructure and Gas-sensing Performance. *Sens. Actuators, B* **2009**, *138*, 113−119.

(19) Fu, H.; Hou, C.; Gu, F.; Han, D.; Wang, Z. Facile Preparation of Rod-like Au/In$_2$O$_3$ Nanocomposites Exhibiting High Response to CO at Room Temperature. *Sens. Actuators, B* **2017**, *243*, 516−524.

(20) Robinson, J. T.; Perkins, F. K.; Snow, E. S.; Wei, Z.; Sheehan, P. E. Reduced Graphene Oxide Molecular Sensors. *Nano Lett.* **2008**, *8*, 3137−3140.

(21) Zhang, B.; Liu, J.; Cui, X.; Wang, Y.; Gao, Y.; Sun, P.; Liu, F.; Shimanoe, K.; Yamazoe, N.; Lu, G. Enhanced Gas Sensing Properties to Acetone Vapor Achieved by α-Fe$_2$O$_3$ Prticles Ameliorated with Reduced Graphene Oxide Sheets. *Sens. Actuators, B* **2017**, *241*, 904−914.

(22) Latif, U.; Dickert, F. L. Graphene Hybrid Materials in Gas Sensing Applications. *Sensors* **2015**, *15*, 30504−30524.

(23) Neri, G.; Leonardi, S. G.; Latino, M.; Donato, N.; Baek, S.; Conte, D. E.; Russo, P. A.; Pinna, N. Sensing Behavior of SnO$_2$/reduced Graphene Oxide Nanocomposites toward NO$_2$. *Sens. Actuators, B* **2013**, *179*, 61−68.

(24) Jie, X.; Zeng, D.; Zhang, J.; Xu, K.; Wu, J.; Zhu, B.; Xie, C. Graphene-wrapped WO$_3$ Nanospheres with Room-temperature NO$_2$ Sensing Induced by Interface Charge Transfer. *Sens. Actuators, B* **2015**, *220*, 201−209.

(25) Yang, W.; Wan, P.; Zhou, X.; Hu, J.; Guan, Y.; Feng, L. Additive-free Synthesis of In$_2$O$_3$ Cubes Embedded into Graphene Sheets and Their Enhanced NO$_2$ Sensing Performance at Room Temperature. *ACS Appl. Mater. Interfaces* **2014**, *6*, 21093−21100.

(26) Kumar, N.; Srivastava, A. K.; Patel, H. S.; Gupta, B. K.; Varma, G. D. Facile Synthesis of ZnO−Reduced Graphene Oxide Nano-composites for NO$_2$ Gas Sensing Applications. *Eur. J. Inorg. Chem.* **2015**, *2015* (11), 1912−1923.

(27) Lu, G.; Ocola, L. E.; Chen, J. Graphene Oxide for Room-Temperature Gas Sensors. *Nanotechnology* **2009**, *20*, 445502−445511.

(28) Choi, S.-J.; Jang, B.-H.; Lee, S.-J.; Min, B. K.; Rothschild, A.; Kim, I.-D. Selective Detection of Acetone and Hydrogen Sulfide for the Diagnosis of Diabetes and Halitosis Using SnO$_2$ Nanofibers Functionalized with Reduced Graphene Oxide Nanosheets. *ACS Appl. Mater. Interfaces* **2014**, *6*, 2588−2597.

(29) Wang, W.; Zhang, Y.; Shen, C.; Chai, Y. Adsorption of CO Molecules on Doped Graphene: A First-principles Study. *AIP Adv.* **2016**, *6*, 025317.

(30) Ma, C.; Shao, X.; Cao, D. Nitrogen-doped Graphene as an Excellent Candidate for Selective Gas Sensing. *Sci. China: Chem.* **2014**, *57*, 911−917.

(31) Li, Y.; Zhao, Y.; Cheng, H.; Hu, Y.; Shi, G.; Dai, L.; Qu, L. Nitrogen-Doped Graphene Quantum Dots with Oxygen-Rich Func-tional Groups. *J. Am. Chem. Soc.* **2012**, *134*, 15−18.

(32) Wang, H.; Maiyalagan, T.; Wang, X. Review on Recent Progress in Nitrogen-Doped Graphene: Synthesis, Characterization, and Its Potential Applications. *ACS Catal.* **2012**, *2*, 781−794.

(33) Wang, Y.; Shao, Y.; Matson, D. W.; Li, J.; Lin, Y. Nitrogen-Doped Graphene and Its Application in Electrochemical Biosensing. *ACS Nano* **2010**, *4*, 1790−1798.

(34) Hummers, W. S.; Offeman, R. E. Preparation of Graphitic Oxide. *J. Am. Chem. Soc.* **1958**, *80* (6), 1339.

(35) Zai, J.; Zhu, J.; Qi, R.; Qian, X. Nearly Monodispersed In(OH)$_3$ Hierarchical Nanospheres and Nanocubes: Tunable Ligand-assisted Synthesis and Their Conversion into Hierarchical In$_2$O$_3$ for Gas Sensing. *J. Mater. Chem. A* **2013**, *1*, 735−745.

(36) Tang, Q.; Zhou, W.; Zhang, W.; Ou, S.; Jiang, K.; Yu, W.; Qian, Y. Size-Controllable Growth of Single Crystal In(OH)$_3$ and In$_2$O$_3$ Nanocubes. *Cryst. Growth Des.* **2005**, *5*, 147−150.

(37) Yin, W.; Su, J.; Cao, M.; Ni, C.; Hu, C.; Wei, B. In$_2$O$_3$ Nanorod Bundles Derived from a Novel Precursor and In$_2$O$_3$ Nanoaggregates: Controllable Synthesis, Characterization, and Property Studies. *J. Phys. Chem. C* **2010**, *114*, 65−73.

(38) Kellici, S.; Acord, J.; Ball, J.; Reehal, H. S.; Morgan, D.; Saha, B. A Single Rapid Route for the Synthesis of Reduced Graphene Oxide with Antibacterial Activities. *RSC Adv.* **2014**, *4*, 14858−14861.

(39) Ou, J.; Zhang, Y.; Chen, L.; Zhao, Q.; Meng, Y.; Guo, Y.; Xiao, D. Nitrogen-rich Porous Carbon Derived from Biomass as a High Performance Anode Material for Lithium Ion Batteries. *J. Mater. Chem. A* **2015**, *3*, 6534−6541.

(40) Xing, Z.; Ju, Z.; Zhao, Y.; Wan, J.; Zhu, Y.; Qiang, Y.; Qian, Y. One-pot Hydrothermal Synthesis of Nitrogen-doped Graphene as High-performance Anode Materials for Lithium Ion Batteries. *Sci. Rep.* **2016**, *6*, 26146.

(41) Chu, D.; Masuda, Y.; Ohji, T.; Kato, K. Shape-Controlled Growth of In(OH)$_3$/In$_2$O$_3$ Nanostructures by Electrodeposition. *Langmuir* **2010**, *26*, 14814−14820.

(42) Yin, W.; Su, J.; Cao, M.; Ni, C.; Cloutier, S. G.; Huang, Z.; Ma, X.; Ren, L.; Hu, C.; Wei, B. In(OH)$_3$ and In$_2$O$_3$ micro/nanostructures: Controllable NaOAc-Assisted Microemulsion Synthesis and Raman Properties. *J. Phys. Chem. C* **2009**, *113*, 19493−19499.

(43) Reddy, T. N.; Manna, J.; Rana, R. K. Polyamine-mediated Interfacial Assembly of rGO-ZnO Nanostructures: a Bio-inspired Approach and Enhanced Photocatalytic Properties. *ACS Appl. Mater. Interfaces* **2015**, *7*, 19684−19690.

(44) Kaur, M.; Jain, N.; Sharma, K.; Bhattacharya, S.; Roy, M.; Tyagi, A. K.; Gupta, S. K.; Yakhmi, J. V. Room-temperature H$_2$S Gas Sensing at ppb Level by Single crystal In$_2$O$_3$ Whiskers. *Sens. Actuators, B* **2008**, *133*, 456−461.

(45) Cai, X.; Shen, X.; Ma, L.; Ji, Z. Facile Synthesis of Nickel−cobalt Sulfide/reduced Graphene Oxide Hybrid with Enhanced Capacitive Performance. *RSC Adv.* **2015**, *5*, 58777−58783.

(46) Peng, S.; Li, L.; Li, C.; Tan, H.; Cai, R.; Yu, H.; Mhaisalkar, S.; Srinivasan, M.; Ramakrishna, S.; Yan, Q. In Situ Growth of NiCo$_2$S$_4$ Nanosheets on Graphene for High-performance Supercapacitors. *Chem. Commun.* **2013**, *49*, 10178−10180.

(47) Pashchanka, M.; Hoffmann, R. C.; Gurlo, A.; Schneider, J. J. Molecular Based, Chimie Douce Approach to 0D and 1D Indium Oxide Nanostructures. Evaluation of Their Sensing Properties towards CO and H$_2$. *J. Mater. Chem.* **2010**, *20*, 8311−8319.

(48) Cao, Y.; Huang, X.; Wu, Y.; Zou, Y.-C.; Zhao, J.; Li, G.-D.; Zou, X. Three-dimensional Ultrathin In$_2$O$_3$ Nanosheets with Morphology-enhanced Activity for Amine Sensing. *RSC Adv.* **2015**, *5*, 60541−60548.

(49) Barry, S. T.; Gordon, P. G.; Ward, M. J.; Heikkila, M. J.; Monillas, W. H.; Yap, G. P. A.; Ritala, M.; Leskelä, M. Chemical Vapour Deposition of In$_2$O$_3$ Thin Films from a Tris-guanidinate Indium Precursor. *Dalton Trans.* **2011**, *40*, 9425−9430.

(50) Rouquerol, J.; Avnir, D.; Fairbridge, C. W.; Everett, D. H.; Haynes, J. M.; Pernicone, N.; Ramsay, J. D. F.; Sing, K. S. W.; Unger, K. K. Recommendations for the Characterization of Porous Solids (Technical Report). *Pure Appl. Chem.* **1994**, *66*, 1739−1758.

(51) Wang, L.; Gao, J.; Wu, B.; Kan, K.; Xu, S.; Xie, Y.; Li, L.; Shi, K. Designed Synthesis of In$_2$O$_3$ Beads@TiO$_2$−In$_2$O$_3$ Composite Nano-fibers for High Performance NO$_2$ Sensor at Room Temperature. *ACS Appl. Mater. Interfaces* **2015**, *7*, 27152−27159.

(52) Arunkumar, S.; Hou, T. F.; Kim, Y. B.; Choi, B. C.; Park, S. H.; Jung, S. H.; Lee, D. W. Au Decorated ZnO Hierarchical Architectures: Facile Synthesis, Tunable Morphology and Enhanced CO Detection at Room Temperature. *Sens. Actuators, B* **2017**, *243*, 990−1001.

(53) Lai, H. Y.; Chen, C. H. Highly Sensitive Room-Temperature CO gas sensors: Pt and Pd Nanoparticle-Decorated In$_2$O$_3$ Flower-Like Nanobundles. *J. Mater. Chem.* **2012**, *22*, 13204−13208.

(54) Singh, N.; Gupta, R. K.; Lee, P. S. Gold-Nanoparticle-Functionalized In_2O_3 Nanowires as CO Gas Sensors with a Significant Enhancement in Response. *ACS Appl. Mater. Interfaces* **2011**, *3*, 2246−2252.

(55) Du, N.; Zhang, H.; Ma, X.; Yang, D. Homogeneous Coating of Au and SnO_2 Nanocrystals on Carbon Nanotubes via Layer-by-Layer Assembly: A New Ternary Hybrid for a Room-Temperature CO Gas Sensor. *Chem. Commun.* **2008**, *618*, 6182−6184.

(56) Dang, L.; Zhang, G.; Kan, K.; Lin, Y.; Bai, F.; Jing, L.; Shen, P.; Li, L.; Shi, K. Heterostructured Co_3O_4/PEI−CNTs Composite: Fabrication, Characterization and CO Gas Sensors at Room Temperature. *J. Mater. Chem. A* **2014**, *2*, 4558−4565.

(57) Joshi, R. K.; Hu, Q.; Alvi, F.; Joshi, N.; Kumar, A. Au Decorated Zinc Oxide Nanowires for CO Sensing. *J. Phys. Chem. C* **2009**, *113*, 16199−16202.

(58) Geng, B.; Zhan, F.; Jiang, H.; Xing, Z.; Fang, C. Facile Production of Self-Assembly Hierarchical Dumbbell-Like CoOOH Nanostructures and Their Room-Temperature CO-Gas-Sensing Properties. *Cryst. Growth Des.* **2008**, *8*, 3497−3500.

(59) Kim, J.-H.; Katoch, A.; Kim, W. H.; Kim, S. S. Realization of ppm-level CO Detection with Exceptionally High Sensitivity Using Reduced Graphene Oxide-Loaded SnO_2 Nanofibers with Simultaneous Au Functionalization. *Chem. Commun.* **2016**, *52*, 3832−3835.

(60) Miao, B.; Zeng, W.; Mu, Y.; Yu, W.; Hussain, S.; Xu, S.; Zhang, H.; Li, T. Controlled Synthesis of Monodisperse $WO_3 \cdot H_2O$ Square Nanoplates and their Gas Sensing Properties. *Appl. Surf. Sci.* **2015**, *349*, 380−386.

(61) Wetchakun, K.; Samerjai, T.; Tamaekong, N.; Liewhiran, C.; Siriwong, C.; Kruefu, V.; Wisitsoraat, A.; Tuantranont, A.; Phanichphant, S. Semiconducting Metal Oxides as Sensors for Environmentally Hazardous Gases. *Sens. Actuators, B* **2011**, *160*, 580−591.

(62) Franke, M. E.; Koplin, T. J.; Simon, U. Metal and Metal Oxide Nanoparticles in Chemiresistors: Does the Nanoscale Matter? *Small* **2006**, *2*, 36−50.

(63) Ding, W.; Wei, Z.; Chen, S.; Qi, X.; Yang, T.; Hu, J.; Wang, D.; Wan, L.-J.; Alvi, S. F.; Li, Li. Space-Confinement-Induced Synthesis of Pyridinic- and Pyrrolic-Nitrogen-Doped Graphene for the Catalysis of Oxygen Reduction. *Angew. Chem., Int. Ed.* **2013**, *52*, 11755−11759.

(64) Lv, R.; Li, Q.; Botello-Méndez, A. R.; Hayashi, T.; Wang, B.; Berkdemir, A.; et al. Nitrogen-doped Graphene: Beyond Single Substitution and Enhanced Molecular Sensing. *Sci. Rep.* **2012**, *2*, 586.

(65) Song, Z.; Wei, Z.; Wang, B.; Luo, Z.; Xu, S.; Zhang, W.; Yu, H.; Li, M.; Huang, Z.; Zang, J.; Yi, F.; Liu, H. Sensitive Room-Temperature H_2S Gas Sensors Employing SnO_2 Quantum Wire/Reduced Graphene Oxide Nanocomposites. *Chem. Mater.* **2016**, *28*, 1205−1212.

(66) Lin, Q.; Li, Y.; Yang, M. Tin oxide/Graphene Composite Fabricated via a Hydrothermal Method for Gas Sensors Working at Room Temperature. *Sens. Actuators, B* **2012**, *173*, 139−147.

(67) Tammanoon, N.; Wisitsoraat, A.; Sriprachuabwong, C.; Phokharatkul, D.; Tuantranont, A.; Phanichphant, S.; Liewhiran, C. Ultrasensitive NO_2 Sensor Based on Ohmic Metal−Semiconductor Interfaces of Electrolytically Exfoliated Graphene/Flame-Spray-Made SnO_2 Nanoparticles Composite Operating at Low Temperatures. *ACS Appl. Mater. Interfaces* **2015**, *7*, 24338−24352.